J. Fluid Mech. (2007), *vol.* 591, *pp.* 155–182.
doi:10.1017/S0022112007007896 Printed in the United Kingdom

Numerical investigation of the tone noise mechanism over laminar airfoils

G. DESQUESNES[1], M. TERRACOL[1] AND P. SAGAUT[2]

[1]Departement of Numerical Simulation and Aeroacoustics, ONERA, 29 av Division Leclerc, BP 72, 92322 Châtillon cedex, France

[2]Institut Jean le Rond d'Alembert, Université Pierre et Marie Curie – Paris 6, Case 162, 4 place Jussieu, 75252 Paris cedex 05, France

(Received 1 August 2006 and in revised form 18 June 2007)

This paper presents the first numerical investigation via direct numerical simulation of the tone noise phenomenon occurring in the flow past laminar airfoils. This phenomenon corresponds to the radiation of discrete acoustic tones in some specific flow conditions, and has received much attention since the 1970s, and several experimental studies have been carried out to identify and understand the underlying physical mechanisms. However, several points remain to be clarified in order to provide a complete explanation of its origin. The flow around a two-dimensional NACA0012 airfoil is considered in order to have a deeper understanding of the tone noise phenomenon. Consistently with previous experimental studies, it is shown that depending on the Reynolds number and angle of attack, two different types of acoustic spectrum are observed: one which exhibits a broadband contribution with a dominant frequency together with a sequence of regularly spaced discrete frequencies, while the other one is only characterized by a simple broadband contribution. The first configuration is typical of the tone noise phenomenon. The present work shows that in this case, the mean flow on the pressure side of the airfoil exhibits a separation bubble near the trailing edge and the main tone frequency is close to the most amplified frequency of the boundary layer. The mechanism proposed in previous works for the main tone generation – which implies the existence of a separation bubble at the pressure side – is therefore validated by numerical simulation. On the other hand, the analysis of the suction side boundary layer reveals that there is no separation and that the most amplified frequency is different from the main tonal one. However, the suction side boundary layer is highly receptive to the tone frequency. Finally, an original explanation for the existence of the secondary discrete frequencies observed in the radiated pressure spectrum is given. They are associated to a bifurcation of the airfoil wake from a symmetric to a non-symmetric vortex pattern. A possible explanation for the existence of this bifurcation is the interaction between the disturbances which are the most amplified by the suction side boundary layer and those originating in the forcing of the suction side flow by the main tone noise mechanism.

1. Introduction

At the beginning of the 1970s, several experiments (Smith *et al.* 1970; Clark 1971; Hersh & Hayden 1971) showed that discrete tones are emitted from isolated airfoils or helicopter rotors in specific flow conditions. Several studies (Paterson, Vogt & Fink 1972; Sunyach *et al.* 1973; Tam 1974; Fink 1975; Arbey & Bataille 1983;

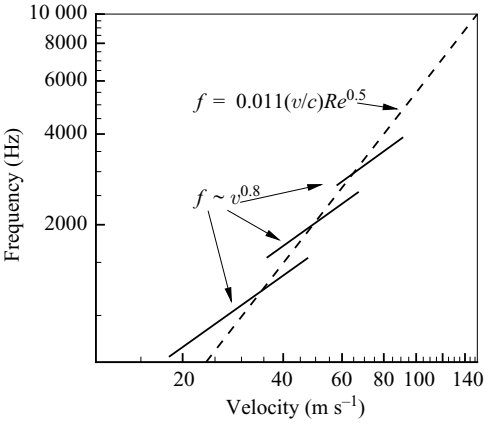

FIGURE 1. Paterson *et al.*'s experimental results. Curves plotted using Paterson *et al.*'s (1972) formula.

Lowson, Fiddes & Nash 1994; Nash & Lowson 1995; Lowson, McAlpine & Nash 1998; McAlpine, Nash & Lowson 1999; Nash, Lowson & McAlpine 1999) have then focused on the understanding of this phenomenon.

A first significant contribution was provided by Paterson *et al.* (1972). Their 10 Hz narrowband measurements on a NACA 0012 and a NACA 0018 two-dimensional airfoil showed undoubtedly the existence of discrete tones which had already been suggested by one-third octave measurements in previous experimental works. They derived an average evolution of the frequency of the discrete tone following the law: $f = 0.011U^{3/2}/(c\nu)^{1/2}$ where c is the chord, U the free-stream velocity and ν the viscosity. They also observed a so-called 'ladder-type' variation of the frequency: locally, the frequency follows a dependence on velocity to the 0.8 power and suddenly undergoes a jump (see figure 1). It was also noted that in some cases, two distinct frequencies can be observed for the same value of viscosity. Paterson *et al.* (1972) proved the phenomenon was linked to the presence of a laminar boundary layer on the pressure side, therefore explaining its disappearance for chord-based Reynolds numbers of around 10^6. No explanations were proposed for the ladder-type variation, but Sharland (1964) suggests that the discrete tone may be linked to a vortex shedding at the trailing edge of the airfoil. The vortex model allows us to find the $f \sim U^{3/2}$ law of the average frequency evolution. However, Sharland did not find the physical size associated to the Strouhal number of 0.2 that characterizes vortex shedding.

Tam (1974) showed the inadequacy of the vortex noise concept and suggested a feedback mechanism to explain the ladder-type structure. Taking the experimental results of Paterson *et al.* (1972), he showed the discrete tonal frequency follows the law: $f = 6.85nU^{0.8}$ where n is an integer. He suggested there was a self-excited feedback loop between the trailing edge and the noise source in the wake. In this scenario, the noise source is induced by boundary-layer instabilities that are amplified at the trailing edge by the acoustic waves. Since a phase condition is necessary for the existence of such a loop, the parameter n is introduced in the evolution of the discrete frequency. This model is qualitatively attractive, however, no experiment has been carried out to support the existence of such a loop.

Another interpretation was proposed by Fink (1975) for the average frequency evolution law proposed by Paterson *et al.* (1972). He assumed that the discrete frequency was linked to the laminar boundary-layer instabilities of the pressure

surface. For convenience, the pressure surface was approximated by a flat plate, and thanks to Shen (1954)'s stability calculation, Fink (1975) could predict Paterson *et al.* (1972)'s experimental formula for the average tonal frequency. However, the flat-plate approximation also makes this result only qualitative.

Arbey & Bataille (1983) carried out new experiments on NACA 0012.8, NACA 0012.16 and NACA* 0012.16 at a 0° angle of attack, to clarify the various proposed theories. Thanks to a low-bandwidth analyser, they showed that the tone peak was actually a superposition of a broadband contribution centred on a main frequency f_s and a set of regularly spaced discrete frequencies f_n. The main frequency f_s was observed to be associated to a Strouhal number of 0.048 ± 0.003 based on the boundary-layer thickness at the trailing edge (numerically computed values from Mari, Jeandel & Mathieu (1976) were used for that purpose). This Strouhal-number value can be predicted by the stability curves of Obremski *et al.* (1969). Therefore, Arbey & Bataille (1983) confirmed Fink (1975)'s assumption that the broadband contribution results from the diffraction, by the trailing edge, of the hydrodynamic fluctuation of the boundary layer identified as Tollmien–Schlichting (T-S) instabilities. To explain the discrete components of the peak, an aeroacoustic feedback mechanism is suggested, analogous to the one described by Tam (1974). This model involves the distance L between the point of maximum velocity and the trailing edge of the airfoil. The proposed evolution law for the discrete components is $f_n = (n + 1/2)KU^{0.85}/L$, where the parameter K was found to be independent of the tested profiles, and Henry (1975)'s numerically computed values were used for L.

Lowson *et al.* (1994) gathered various experimental data to define a pattern in the Reynolds number/angle of attack plane where discrete tones appear in the acoustic spectrum from a NACA 0012 airfoil. They observed that TS waves occur in the boundary layer at lower Re than the first appearance of tone noise. This observation therefore indicates that the presence of instabilities in the boundary layer of the airfoil is not a sufficient condition for the tone noise phenomenon to occur. By performing some calculations of boundary layers of a NACA 0012 profile at 0°, and experiments in a wind tunnel on NACA 0012 and NACA 23015 airfoils, they showed that the appearance of the discrete tones was correlated to the presence of a bubble at the pressure side of the profile. Besides, the intensity of the discrete frequency is correlated to the length of this bubble. They suggested that after the laminar separation, the shear layer acts as an amplifier of the incoming T-S instabilities. This explains the evolution of the tone intensity depending on the velocity for a constant angle of attack: increasing, plateau, decreasing.

Nash *et al.* (1999) conducted new experiments on NACA 0012 airfoils. Thanks to LDA (laser-Doppler anemometry) measurements, they observed that a substantial region of reversed flow could be present on the pressure surface with no tone present in the acoustic spectrum. Besides, they observed only one discrete frequency in a tone case. Flow visualizations showed a regular vortex street shed from the trailing edge for the tone case. Spatial linear instability analysis could predict the tone frequency and, calculation showed that the highest spatial amplification coefficient in the no-tone case was much lower than that in the tone case. In their conclusion, the authors confirmed the major role of the boundary-layer instabilities on the pressure surface in the tone noise phenomenon and suggested a revised feedback loop mechanism for the tone noise generation.

At the same time, and using the same methodology for the linear instability analysis, McAlpine *et al.* (1999) showed that the tone frequency is also close to the most amplified frequency on the pressure side for other experimental configurations.

This result is in agreement with the mechanism suggested by Nash *et al.* (1999). However, McAlpine *et al.* (1999) suggest that the vortex shedding at the pressure side owing to the separation bubble acts in a similar way to the vortex shedding behind a cylinder. For this case, Koch (1985) showed that there is a small region of absolute instability close to the body, which explains why the vortex shedding is a self-excited mechanism. Such a mechanism can therefore not be excluded in the tone noise case according to McAlpine *et al.* (1999).

It therefore appears that since the 1970s, great improvements have been made in the understanding of the tone noise phenomenon. However, several issues remain open. Since Arbey & Bataille (1983), no experimental investigation of the suction side flow properties has been performed although it was suggested that it may be involved in the feedback-loop mechanism. The origin of the secondary peaks in the radiated acoustic spectrum has not been investigated since this study and remains unknown. The possible interactions between the disturbances coming from both sides of the airfoil in the trailing-edge region have never been studied.

All previous works dealing with the tonal noise phenomenon rely on theoretical models and wind tunnel experiments. In order to obtain a deeper insight into the physics of the tone noise mechanism, direct numerical simulations have been carried out in the present work for different configurations of the flow past a NACA0012 airfoil. They have been done in two dimensions because the assumption was made that the governing mechanisms of tonal noise are essentially two-dimensional. This assumption is based on the results of previous experiments. In particular, Paterson *et al.* (1972) showed that pressure side fluctuations were coherent to a large extent in the spanwise direction.

The paper is organized as follows §2 presents the mathematical model and numerical schemes that have been retained for the study. Section 3 describes the different configurations under consideration. In §4, it will be shown that depending on the Reynolds number and the angle of attack, two different types of acoustic spectrum can be observed. One shows a broadband contribution with a dominant frequency and a sequence of discrete frequencies as observed by Arbey & Bataille (1983) for a tonal noise configuration. The second one displays, however, a broadband noise where no discrete frequencies can be observed. In §5, a study of the mean flow by a linear instability analysis will be performed. It will be shown that the main tone frequency is close to the most amplified frequency of the pressure side's boundary layer, but different from that of the suction side. Then in §6, a different interpretation from that of Arbey & Bataille (1983) will be proposed to explain the discrete frequency components present in the tone noise spectrum. The equidistance between the discrete frequencies will be interpreted as being due to the amplitude modulation of the dominant broadband contribution frequency of the spectrum. Some visualizations of the flow will make it possible to explain this modulation as a periodic cycle of phasing/anti-phasing of the instabilities of the pressure and suction sides at the trailing edge.

2. Mathematical model and numerical methods

The direct numerical simulation of the tone noise mechanism is performed solving the system of the compressible Navier–Stokes equations in two dimensions. The temperature, T, the pressure, P, and the density, ρ, are linked by the perfect gas state law: the iso-volume heat coefficient, C_v, is set to $717.5\ \mathrm{m^2\,s^{-2}\,K^{-1}}$ and $\gamma = 1.4$ (the ratio of specific heats). Stokes' assumption is used to express the viscous stress tensor,

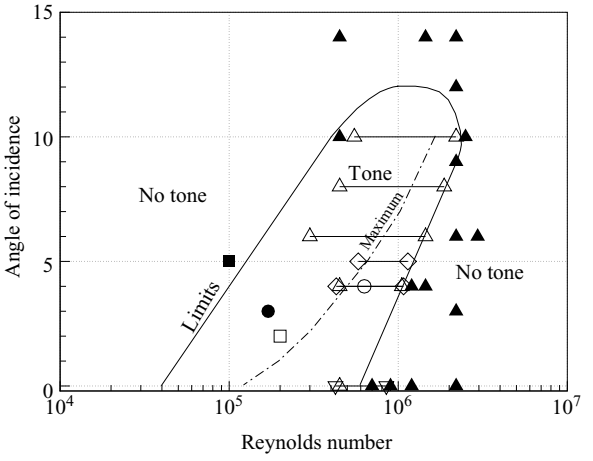

FIGURE 2. Pattern proposed by Lowson *et al.* (1994) in which the tonal noise phenomenon is likely to occur. The two squares indicate the flow configurations retained for the present numerical study. Open symbols correspond to configurations in which the tone noise phenomenon has been observed, while it was not present in the configurations corresponding to filled symbols. □, Case 1; ■, Case 2; △, Paterson *et al.* (1972) tone; ▲, Paterson *et al.* (1972) no tone; ▽, Arbey *et al.* (1983) no tone; ◇, Lowson *et al.* (1994) tone; ○, Lowson *et al.* (1998) tone; ●, Lowson *et al.* (1998) no tone.

and Sutherland's law is used to compute the viscosity, μ, as a nonlinear function of T. Finally, the thermal conductivity coefficient, κ, is linked to viscosity through the use of a Prandtl number assumption ($Pr = 0.7$ in this study).

High-order numerical schemes have been retained to discretize the Navier–Stokes equations. The spatial scheme used here relies on a classical sixth-order accurate centred explicit finite-difference discretization, whereas a compact explicit third-order accurate Runge–Kutta algorithm is used for time advancement. A tenth-order accurate symmetric linear filter is applied on the flow variables at each time step to prevent the occurrence of spurious wiggles. Finally, the curvilinear extension strategy proposed by Visbal & Gaitonde (2002) has been retained to handle complex geometries. See Desquesnes *et al.* (2006) for further details on the numerical method which has been extensively used for both aerodynamic and acoustic computations.

A standard no-slip condition is enforced at the airfoil surface. In order to prevent numerical reflections at the boundaries of the computational domain, the non-reflective boundary condition developed by Thompson (1987) has been implemented. In addition, a sponge area is employed to damp the flow fluctuations before they reach the boundaries of the domain. This sponge area consists in a progressive stretching of the computational grid in the direction normal to the far-field boundaries along with a decrease in the order of the linear filter.

3. Simulation configurations

A NACA0012 airfoil with a chord of 0.3 m has been selected since this was the most used in previous experimental studies. Two specific configurations (with and without tone noise) have been chosen using the diagram constructed by Lowson *et al.* (1994) (see figure 2) which displays the region in the Reynolds number/angle of attack plane in which the tone noise phenomenon is expected.

	Reynolds number	Angle of attack (deg.)	Mach number	Tone noise expected
Case 1	2×10^5	2	0.1	Yes
Case 2	1×10^5	5	0.05	No

TABLE 1. Flow characteristics of the two chosen configurations.

	Number of cells	Refinement	h/c	d/c
Mesh 1	2196×202		7.2×10^{-4}	6.0×10^{-3}
Mesh 2	2196×404	Wall-normal direction	3.8×10^{-4}	6.0×10^{-3}
Mesh 3	2196×225	Wall-normal direction*	3.8×10^{-4}	6.0×10^{-3}
Mesh 4	4392×225	Tangent direction	3.8×10^{-4}	3.0×10^{-3}

TABLE 2. Characteristics of the four grids used; the third column indicates the refinement by 2 in one direction compared to Mesh 1. *, refinement limited to the boundary-layer area. h is the height of the first cell on the airfoil, d the width of the last cell at the suction side near the trailing edge.

This diagram was derived from the experimental data of Paterson *et al.* (1972) and those from a series of studies performed at NASA Langley on the aerofoil self-noise problem, summarized in Brooks, Pope & Marcolini (1989). From this figure, it appears that the tone noise phenomenon has been observed for a wide range of Reynolds numbers and angles of attack. It can therefore be thought that there exist several different fundamental mechanisms which lead to this phenomenon. However, the different experiments carried out at low angle of attack and moderate value of the Reynolds number exhibit some similar flow features; it can thus be expected that there exists a unique mechanism responsible for the tone noise generation in such flow configurations. The present study will focus on these flows. The flow parameters of the two selected configurations, hereinafter referred to as Case 1 and Case 2 are summarized in table 1 and are also displayed in figure 2. Tone noise is expected for Case 1 whereas it is not for Case 2. The Reynolds number is based on the free-stream velocity, u_∞, and density, ρ_∞, and on the chord of the airfoil, c.

It is to be noted that the corresponding simulations will be performed in two dimensions. According to the previous works, the hypothesis is that the inherent mechanism of the tone noise phenomenon is two-dimensional. Paterson *et al.* (1972) showed that the tone noise did not appear when the boundary layer on the pressure side was not laminar. Moreover, correlation measurements exhibited a long-range correlation of the pressure side fluctuations in the spanwise direction. Although in the two selected configurations the flow is not expected to remain rigorously two-dimensional over the entire computational domain, it is reasonable to think that two-dimensional simulations will be sufficient to provide a better understanding of the tone noise mechanism.

Four different computational grids, Mesh 1 to Mesh 4, have been considered in order to check the influence of grid resolution. Mesh 2 to Mesh 4 have been built by successive refinement (by a factor of 2) of Mesh 1. Mesh 3 has been constructed by refining only the boundary-layer region in the wall-normal direction, a geometric progression being used away from it. The main features of the meshes are summarized in table 2 where h indicates the height of the first cell close to the airfoil, and d the width of the last cell on the airfoil surface at the suction side near the trailing edge. They have been designed so that the grid lines remain orthogonal to the airfoil surface.

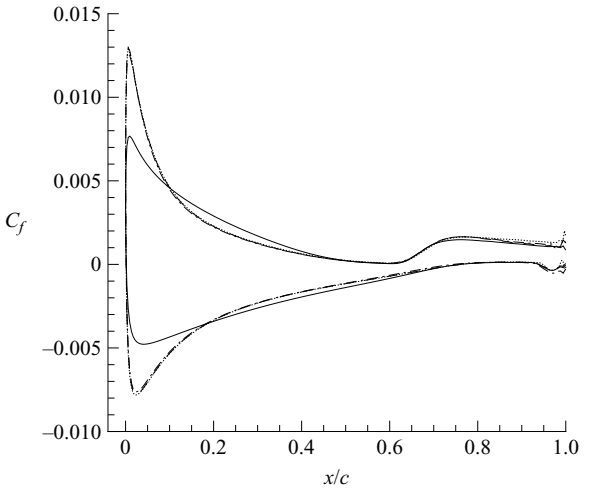

FIGURE 3. Friction coefficient, C_f, computed for Case 1 on ——, Mesh 1; - - -, Mesh 2; –•–, Mesh 3; · · ·, Mesh 4 – negative value of C_f for the pressure side.

The time step of the simulation is 0.7250 μs for Mesh 1 whereas it is 0.3625 μs for Mesh 2 to Mesh 4. The statistical steady state of the flow is reached after 100 000 time steps for Mesh 1 and 200 000 for the other meshes. The statistical moments are then computed over the same period. Over the same time, a temporal pressure signal is extracted at $0.5c$ above the trailing edge from each grid.

The study of the mean flow features shows that results are grid-independent for Mesh 2 to Mesh 4. This is illustrated looking at the skin friction coefficient distribution, C_f, computed on each grid (see figure 3). Errors observed on Mesh 1 are linked to the discretization in the wall-normal direction in the boundary-layer region. Grid convergence is also observed on the time Fourier spectrum of the solution. The most amplified frequency is 993 Hz for Mesh 1 whereas it is 831 Hz for Mesh 2 to Mesh 4 – the frequency resolution of the Fourier transform being 14 Hz. According to these results, Mesh 3 is selected for further analysis in this paper. For Case 2, mesh convergence was observed between Mesh 1 and Mesh 3 showing the last grid is suitable for the simulation of this case.

The statistical moments for Case 1 and Case 2 have been computed collecting samples over 500 000 time steps, corresponding to a physical sampling time of 0.18 s. This sampling time corresponds to 149 periods of the characteristic frequency of Case 1 and 45 periods for Case 2 – more details about these frequencies will be given in § 4. For both simulations, additional data processing is carried out using virtual probes. For these probes, data sampling has been performed every 44 time steps. The associated time step is 15.95×10^{-6} s or equivalently $18.44 \times 10^{-3}\, c/a_0$. About 34 000 samples have been collected, corresponding to a sampling time length of 0.54 s, or $627\, c/a_0$. This is equivalent to about 450 and 135 periods of the characteristic frequency for Cases 1 and 2, respectively.

4. Main flow features

This section gives a first analysis of the two simulated cases, and highlights their main physical features.

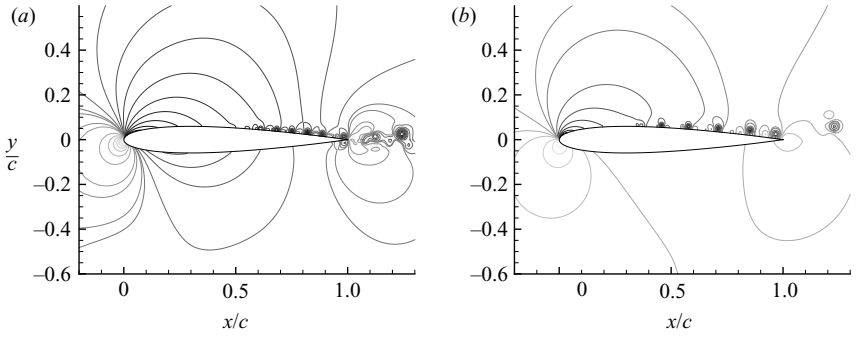

FIGURE 4. Instantaneous iso-pressure contours. (*a*) Case 1; (*b*) Case 2.

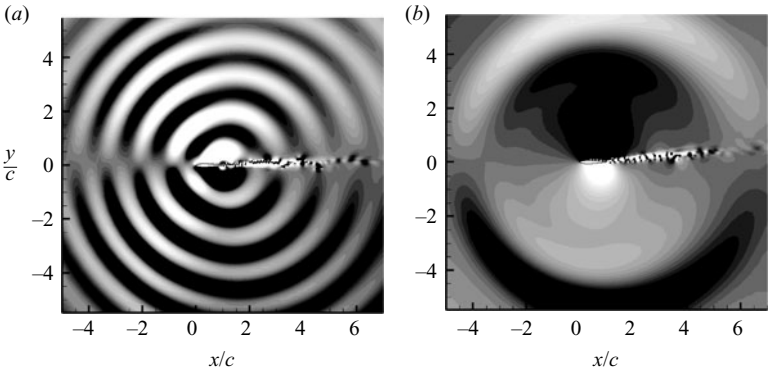

FIGURE 5. Instantaneous pressure fluctuations. (*a*) Case 1 (contours between −5 and 5 Pa); (*b*) Case 2 (contours between −2 and 2 Pa).

4.1. *Instantaneous flow*

Figure 4 displays a view of the instantaneous pressure field for the two considered cases once the statistically steady state has been reached. Some instabilities can be seen on the suction side for both the simulations. They look stronger and appear earlier for Case 2 than for Case 1. Their spatial period is also larger for Case 2. However, some perturbations can be observed at the pressure side near the trailing edge only for Case 1. Figure 5 shows an instantaneous field of the pressure fluctuations for both simulations. It can be seen that in both cases, the main acoustic source is located in the wake in the vicinity of the trailing edge. It can also be seen that the apparent frequency of the acoustic waves is larger in Case 1 than in Case 2. Moreover, the amplitude of the pressure fluctuations is significantly larger for the first simulation – the grey level variations are associated to a larger interval for this simulation.

Pressure–time history is stored for analysis at six different virtual probes: points 1, 2 and 3 are located 0.5, 1.0 and 2.0 chord above the trailing edge, respectively, points 4, 5 and 6: 0.5, 1.0 and 2.0 below it, respectively. Since the virtual probes are located far away from the region in which hydrodynamic fluctuations are observed, the extracted fluctuations can be considered as purely acoustic. The analysis reveals that two sets can be defined: one for points 1, 2 and 3; the other for points 4, 5 and 6. For each set, the amplitude is the only feature that distinguishes the signals, the observed frequency being the same. Table 3 displays the *rms* (root mean square of the fluctuation) of pressure measured at each point for each simulation. What was

	rms pressure (dB)	
	Case 1	Case 2
Point 1	112.2	101.4
Point 2	108.6	98.7
Point 3	104.8	95.8
Point 4	112.3	101.5
Point 5	108.7	98.7
Point 6	104.9	95.8

TABLE 3. Root mean square pressure (dB) at the extraction points for Cases 1 and 2.

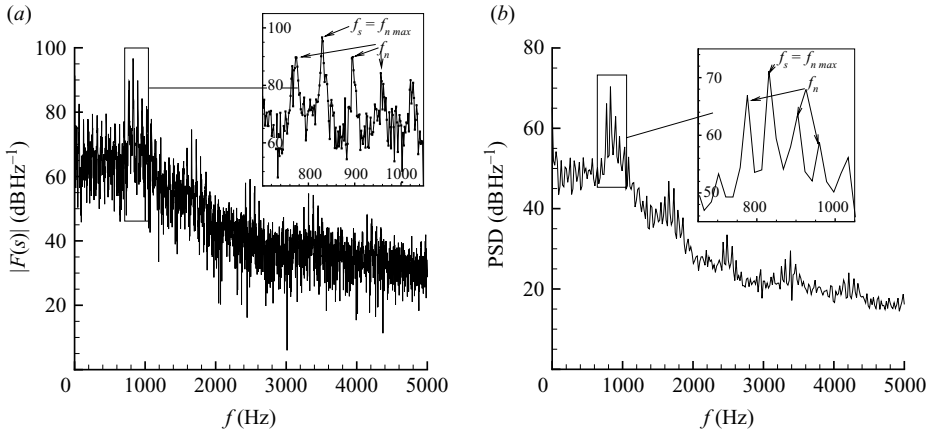

FIGURE 6. Case 1, point 1: (*a*) modulus of the Fourier transform in dB depending on the frequency on the interval 0–5 kHz; (*b*) estimated PSD on the interval 0–5 kHz.

observed qualitatively is confirmed here: Case 1 noise level is much larger than Case 2 noise level.

The tone noise phenomenon is characterized by a particular spectrum shape. Figure 6(*a*) displays the Fourier transform of the pressure signal extracted at point 1 for Case 1. The frequency resolution is equal to 1.84 Hz. This spectrum exhibits a set of discrete frequencies which dominate the spectrum. The main peak, f_s, which appears near 800 Hz, has an intensity which is 20 dB above the background noise. This is consistent with the experimental observations from Arbey & Bataille (1983) and Nash & Lowson (1995). The other groups of discrete frequencies seem to be some harmonics of the first one. Both the frequency and the intensity of the main peak of each group are given in table 4. From this table, it can be concluded that the secondary peaks are indeed harmonics of the first one. A careful analysis of figure 6(*a*) shows that the discrete frequencies f_n of a group are uniformly distributed. The frequency spacing between two discrete peaks Δf is constant and of the order of 64 Hz. Therefore, the main frequency f_s is identified as the discrete frequency with the highest intensity, $f_{n\,max}$. Arbey & Bataille (1983) made the same observations, and their notation will be used hereinafter. Strong variations are present in the acoustic spectrum, showing that the acoustic signal is not purely periodic, and that one of the components of the signal is random. In order to assess the previous results, a statistical approach must be used to analyse the signal. First, it is considered as a

		Peak 1	Peak 2	Peak 3	Peak 4	Peak 5
Point 1	frequency (Hz)	830	1659	2488	3318	4147
	intensity (dB)	96	74	59	55	48
	difference (Hz)	—	829	829	830	829
Point 2	frequency (Hz)	829	1659	2486	3318	4147
	intensity (dB)	93	71	56	52	47
	difference (Hz)	—	830	827	832	829
Point 3	frequency (Hz)	829	1659	2486	3318	4147
	intensity (dB)	89	67	52	42	31
	difference (Hz)	—	830	827	832	829
Point 4	frequency (Hz)	829	1659	2488	3318	4145
	intensity (dB)	97	75	59	58	50
	difference (Hz)	—	830	829	830	827
Point 5	frequency (Hz)	829	1659	2486	3318	4147
	intensity (dB)	93	72	55	55	47
	difference (Hz)	—	830	827	832	829
Point 6	frequency (Hz)	829	1659	2486	3318	4147
	intensity (dB)	89	68	51	45	31
	difference (Hz)	—	830	827	832	829

TABLE 4. Characteristics of the peaks in the acoustic spectrum for Case 1. 'Difference' refers to the frequency spacing from the previous peak.

statistically steady and ergodic function. Then its power spectral density (PSD) can be estimated with the periodogram method. It consists in dividing the sample set into N subsets, computing the Fourier transform of each subset and averaging the square modulus of the Fourier transform. The PSD of the signal at probe 1 has been estimated using 10 blocks and is displayed for Case 1 in figure 6(b), with an associated frequency resolution equal to 18.7 Hz. As can be seen, one of the consequences of the periodogram method is to decrease the intensity levels. However, it can be seen that the same groups of discrete frequencies as in the Fourier transform are observed on the PSD plot. That shows they are the inherent features of the signal. The analysis of the spectrum of the acoustic signal of Case 1 therefore clearly demonstrates that its characteristics match those of the tone noise phenomenon.

The Fourier transform of the acoustic signal at point 1 for Case 2 is shown in figure 7(a) for frequencies between 0 and 2500 Hz. This a typical broadband spectrum is centred around 260 Hz. It appears very irregular and the statistical approach is necessary to analyse it. The PSD is estimated with 10 blocks (figure 7b). The broadband peak centred on 260 Hz can be observed with a harmonic at 520 Hz, but no discrete frequency appears on the graph. From this analysis, we conclude that the acoustic signal of Case 2 does not exhibit the features of the tone noise phenomenon.

On the basis of the analysis of the acoustic signals performed in this section, and the definition given to the tone noise phenomenon in previous experimental studies, Case 1 will be hereinafter referred to as 'tone case' and Case 2 to 'no-tone case'. In the following sections, the flow will be more deeply investigated in order to compare the mechanisms involved with experimental observations.

4.2. *Mean flow analysis*

The friction coefficient, C_f, is shown in figure 8. For Case 1, the C_f curve exhibits a sudden change of slope at 60 % of the chord on the suction side. At this location, the

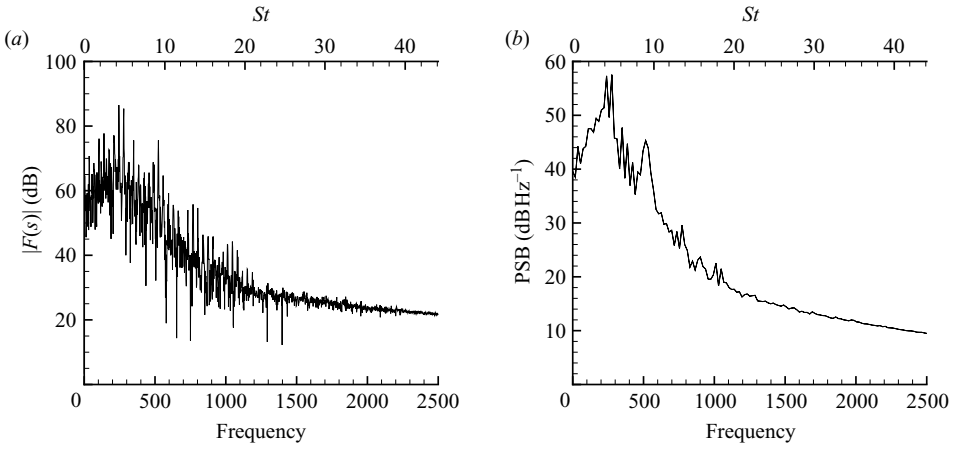

FIGURE 7. Case 2, point 1: (*a*) modulus in dB of the Fourier transform depending on the frequency and the Strouhal number on the interval 0–2.5 kHz; (*b*) estimated PSD.

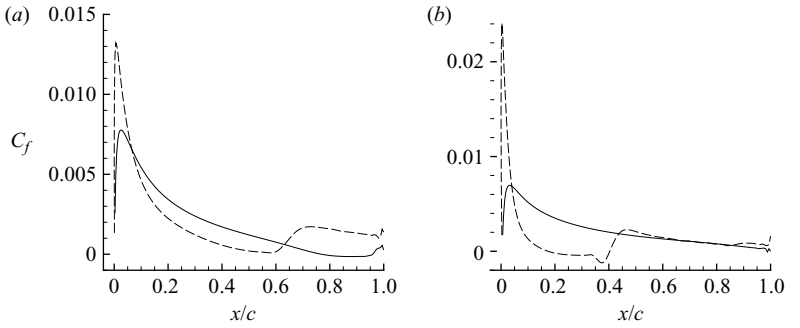

FIGURE 8. Friction coefficient C_f for (*a*) Case 1 and (*b*) Case 2: – – –, suction side; ——, pressure side.

curve indicates that the boundary layer comes close to separation. The point where the friction coefficient vanishes is usually referred to as the marginal separation point (Stewartson, Smith & Kaups 1982). Goldstein, Leib & Cowley (1987) showed that instabilities of the Tollmien–Schlichting wave type can be generated at such a point which is highly receptive to external disturbances – this will be discussed in more detail in § 5.2. On the pressure side, separation occurs at 76 % of the chord whereas the flow reattaches at 96 % as observed by Lowson *et al.* (1994). For Case 2, it can be seen that the boundary layer separates at 18 % on the suction side and reattaches at 40 %. It is worth noting that the friction coefficient in the recirculation region has the same features as those reported by Alam & Sandham (2000) in the two-dimensional simulation of a short laminar bubble which exhibits self-sustained vortex shedding, and is significantly different from that of the numerical simulation of a separated turbulent boundary layer (Na & Moin 1998). It can be noticed that no separation point is observed on the pressure side. Lowson *et al.* (1994) showed that the tone noise phenomenon is linked to the presence of a laminar separation bubble on the pressure side of the airfoil. Then, Nash *et al.* (1999) characterized the mean flow on this side near the trailing edge. The purpose is here to compare our results with the experimental ones. Hereinafter, u_t will refer to the tangential component of the

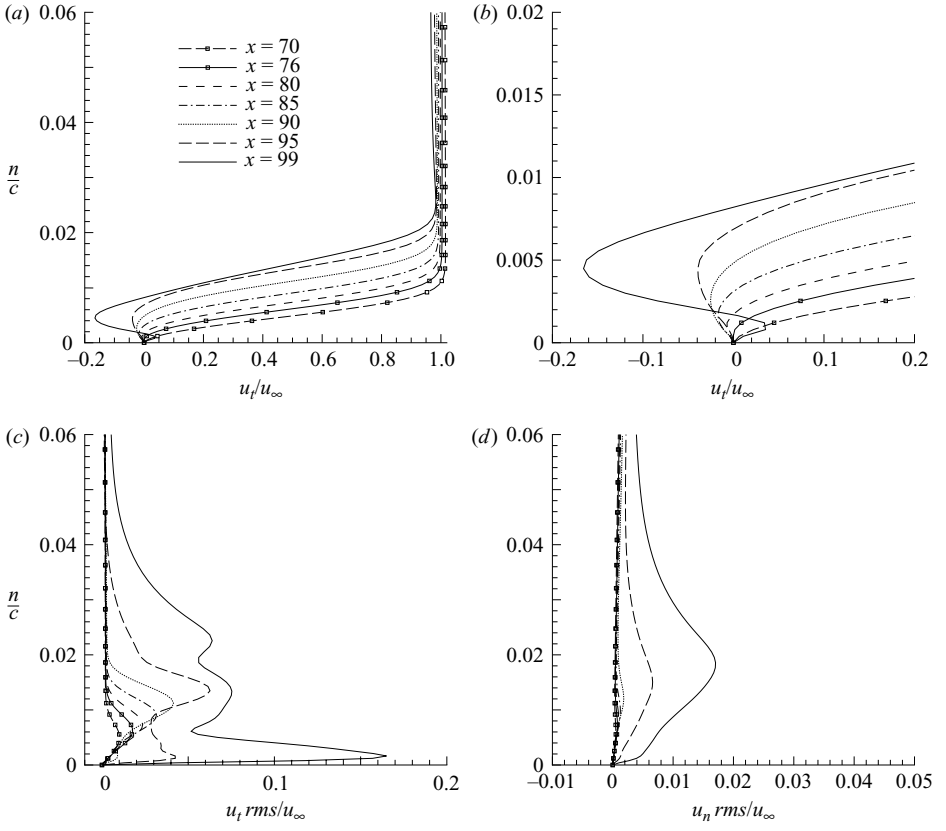

FIGURE 9. Mean and *rms* profiles of Case 1, pressure side – n is the distance to the wall. x is percentage of the chord.

velocity vector with respect to the airfoil's surface (positive values in the streamwise direction). The wall normal component is denoted by u_n.

Figure 9 show the mean and *rms* profiles of the velocity components on the pressure side for Case 1. At 70 % of the chord, where the boundary layer remains attached and laminar, the *rms* profiles of u_t exhibit one peak at half the boundary-layer thickness. It can be seen that the separation bubble (from 76 % of the chord) is responsible for a strong amplification of the *rms* levels of u_t. Near the trailing edge, after the reattachment point at 96 %, it can be seen on the u_t profiles that the mean flow passes from a region of reversed flow back to the streamwise direction before approaching zero near the surface. Simultaneously, the *rms* profile of u_t exhibits a triple-peak distribution throughout the bubble thickness. Figure 9 shows that this triple-peak distribution for *rms* of u_t appears only in the last 10 % of the chord before the trailing edge. Up to 90 % of the chord, the wall-normal velocity fluctuations are not significant. They, however, become significant in the last 10 % of the chord before the trailing edge. This region is the same as that where the triple-peak distribution for the *rms* profile of u_t is observed. Nevertheless, the amplitude of the *rms* profiles of u_n remain much lower than those of the tangential velocity fluctuations.

Similar observations have been reported by Nash *et al.* (1999) in their study on the mean and *rms* profiles dealing with the existence of the following flow features: laminar separation bubble, triple-peak distribution for the *rms* tangent velocity profile

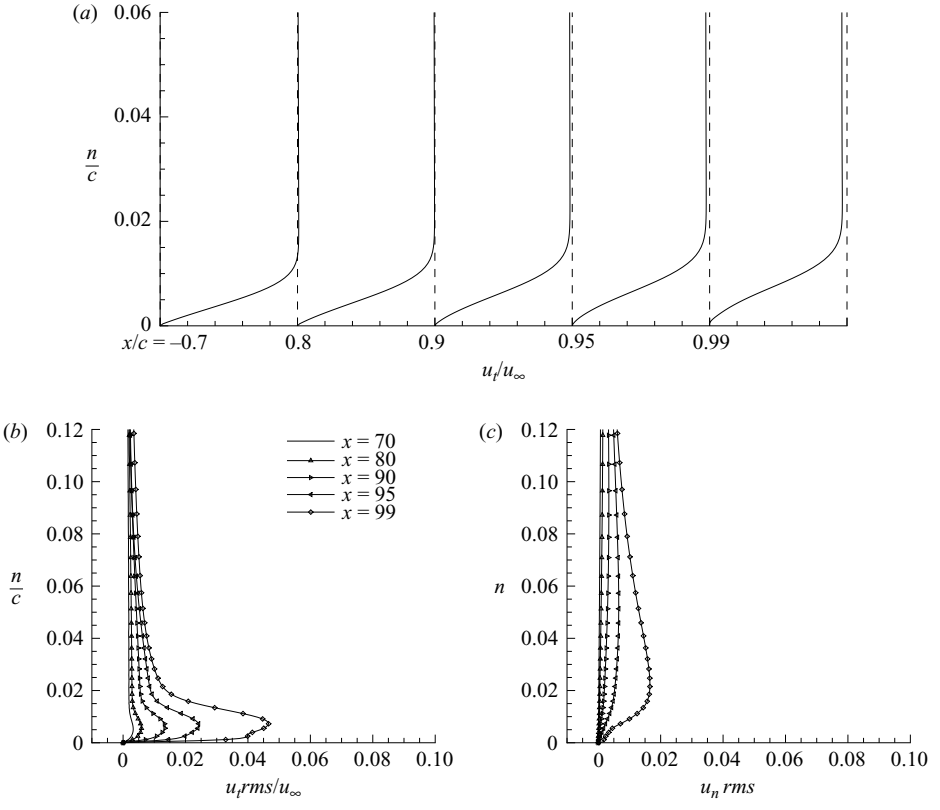

FIGURE 10. Mean and *rms* profiles of Case 2 on the pressure side – n is the distance to the wall x percentage of chord.

and particular mean tangential velocity profile downstream of the reattachment point. It therefore appears that the simulation of Case 1 reproduces clearly the main flow features found to be involved in the tone noise generation in previous experimental studies.

Figure 10 displays the mean and *rms* profiles of velocity components for different chordwise positions on the pressure side for Case 2. As predicted by the C_f curve, no separation point can be observed on the mean velocity profiles. The *rms* profile of the tangent velocity exhibits a single peak distribution with a maximum located at about half of the boundary-layer thickness. No amplified instabilities can be observed on this side unlike in Case 1. This result is in agreement with Lowson *et al.* (1994)'s assumption that the presence of a laminar separation bubble on the pressure side is a necessary condition for the tonal noise to occur.

A detailed analysis of the flow on the suction side has never been reported in the experimental studies. However, in the conclusion of their experimental studies on airfoil placed at a 0° angle of attack, Arbey & Bataille (1983) suggested that the feedback mechanism seems to involve the suction side in the case of an airfoil at non-zero angle of attack. Our purpose is to clarify this point.

It was noticed on the C_f distribution for Case 1 (figure 8) that the mean flow comes close to separation between 40 % and 60 % of the chord on the suction side. Figure 11 shows the mean tangential velocity profile for $x = 40\,\%$, 50 % and 60 %. It can be seen that all these profiles present an inflection point, which is a necessary

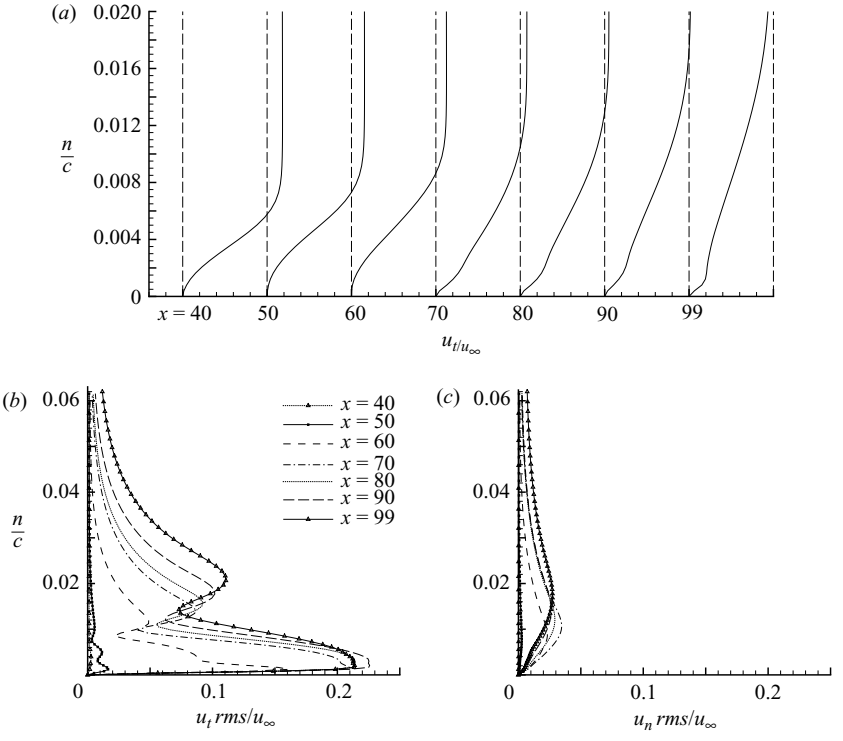

FIGURE 11. Mean and *rms* profiles of Case 1, suction side – n is the distance to the wall. x is percentage of chord.

condition for inviscid instabilities to appear provided that this inflection point is far enough away from the wall (McAlpine *et al.* 1999). Mean profiles after $x/c = 0.6$ exhibit a specific shape which seems to indicate the presence of such instabilities. This is confirmed by looking at the *rms* profiles of the tangent velocity which present some high levels downstream of $x/c = 0.6$. All the profiles located downstream of $x/c = 0.6$ are characterized by a two-peak distribution, and the maximum value of the *rms* profile at $x/c = 0.99$ reaches 22 % of u_∞. The intensity of the *rms* profiles of u_t seems to indicate that the flow in Case 1 should become three-dimensional when approaching the trailing edge. However, considering the Reynolds number of Case 1 ($Re = 200\,000$), and that the amplitude of the wall-normal fluctuations is much lower, it is believed that the flow would not lead to a full transition and would keep a strong coherence in the spanwise direction. So it is assumed that this two-dimensional simulated flow is sufficient to perform a physical analysis of the phenomena involved in tone noise. Since the 1990s, the flow on the suction side of the airfoil has not been deeply investigated in wind tunnel experiments, and therefore these instabilities have not been taken into account to explain the tone noise phenomenon. The role they play in tone noise generation is therefore a question that remains to be answered. It will be addressed below.

The mean velocity profiles plotted in figure 12 confirm that there is a separation point on the suction side at 18 % of the chord and a reattachment point at 40 % for Case 2. The *rms* profiles show that there are amplified instabilities in the boundary layer of the suction side. It is seen that the separation bubble is responsible for the highest amplification of the instabilities and it is correlated to the inflection points of

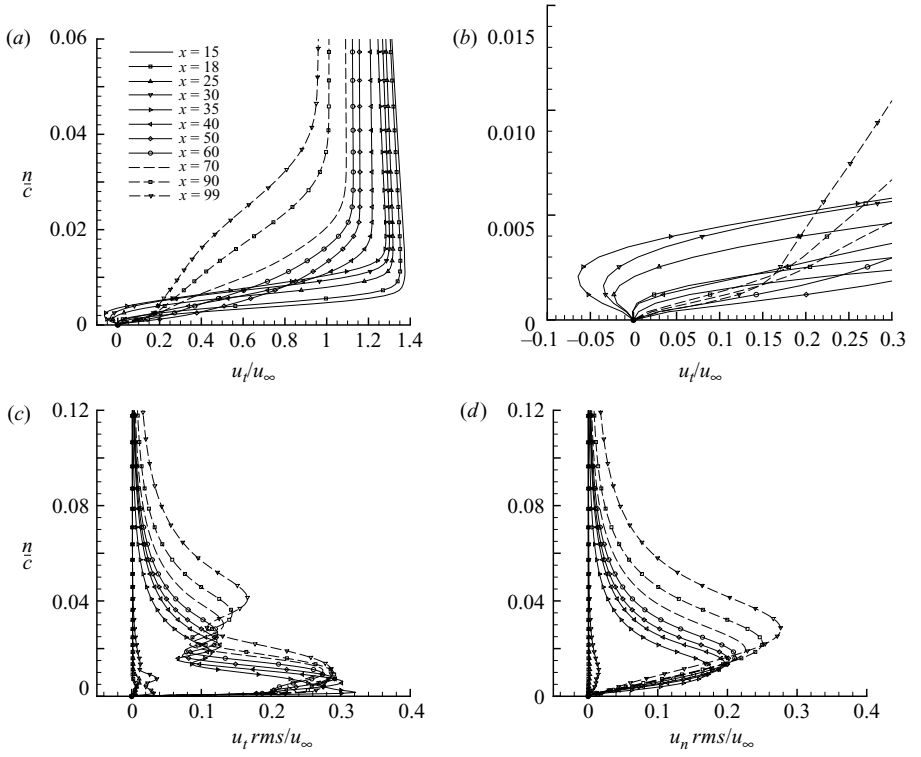

FIGURE 12. Mean and *rms* profiles of Case 2 suction side – n is the distance to the wall. x is percentage of chord.

the mean velocity profiles in the bubble. In their simulation, Alam & Sandham (2000) demonstrated that separation bubbles with strong reverse flow (more than 15 % of the external velocity) exhibit characteristics of absolute instability. In the present case, the maximum of reverse flow is less than 7 % of u_∞ (at $x/c = 0.37$), showing that the separation bubble acts as a noise amplifier and not as a noise generator. Therefore, absolute instability is probably not the origin of the vortex shedding in the present case. After the reattachment point, the *rms* profiles of u_t exhibit a two-peak distribution. The variations of the *rms* profiles of u_n are of the same order as those of the tangent component. These intensities suggest that the flow may also become three-dimensional at this location.

4.3. *Conclusion*

For Case 1 and Case 2, it was shown that the features of the mean flow on the pressure side are in agreement with experimental observations. Besides, amplified instabilities have been observed on the suction side for both cases. The flow physics on this side have not been investigated in experiments up to now, therefore the influence of these instabilities on the tone noise phenomenon remains to be investigated. In the following, the emphasis is on Case 1, the purpose being to understand precisely the mechanism responsible for the tone noise phenomenon.

5. Main tone noise frequency (f_s) generation

A wall pressure signal has been extracted at the computational points located in the last 20 % of the chord upstream of the trailing edge on both the pressure and

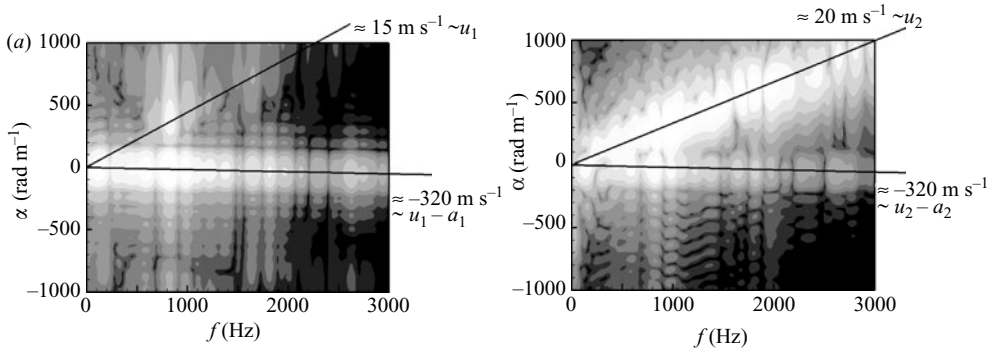

FIGURE 13. Fourier transform in space and in time for a wall pressure signal extracted on (*a*) the pressure side and (*b*) on the suction side, log of the modulus of the coefficients is presented in grey scale. u_1 is the advection velocity of hydrodynamic fluctuations on the pressure side, a_1 the sound velocity; u_2 is the advection velocity on the suction side, a_2 the sound velocity.

suction sides. The sampling time is about 15 periods of the main tone noise frequency. Frequency/wavenumber spectra have then been computed from these signals, which are displayed on figure 13 (*a*, *b*). Such a transform makes it possible to identify the different advection velocities of the fluctuations present in a signal. On each graph, two different velocities can be observed. The nearly horizontal line corresponds to propagation at acoustic velocity in the upstream direction while the other one is characterized by a velocity which is of the order of the typical convection speed in the boundary layer. Therefore, the latter is associated to hydrodynamic fluctuations. The peak associated to the main tonal frequency (830 Hz) can be observed on the two types of fluctuations. From this observation, it can be concluded that the acoustic signal and the hydrodynamic fluctuations in the boundary layer at the pressure and suction sides are strongly correlated.

In several studies dealing with the tone noise phenomenon, it was attempted to predict analytically the tone noise frequency by calculating the stability characteristics of the flow. Up to now, it has always been necessary to model the boundary-layer profile for the computation. For that purpose, Tam (1974), Fink (1975, 1978), Longhouse (1977) and Arbey & Bataille (1983) used the flow over a flat plate assuming zero pressure gradient to model the boundary layer of the airfoils. Archibald (1975) selected the Hartree profile to model the pressure gradient downstream of the midchord of an airfoil. These approaches showed that the tone noise frequency was of the same order as the frequency of the most amplified hydrodynamic perturbations inside the boundary layer. An improved approach was proposed by Nash *et al.* (1999) and McAlpine *et al.* (1999) to model the boundary layer at different chordwise stations all along the pressure side of the airfoil. At selected stations, the shape factor, H, is estimated from experimental measurements, and extrapolated at different chordwise stations in order to use a Hartree profile with the same shape factor to model the boundary layer. In the present direct numerical simulation, the mean flow is known at each point of the computational grid and the instability analysis can therefore be performed easily at a large number of stations along the airfoil. Using our numerical results, the generation of boundary-layer instabilities has been studied over the airfoil pressure and suction sides for Case 1. Spatial analyses have been carried out by solving the incompressible Navier–Stokes (iNS) equations in a perturbation form. For a given profile, the spatial growth rate, $-\alpha_i$, associated to a frequency f has been computed.

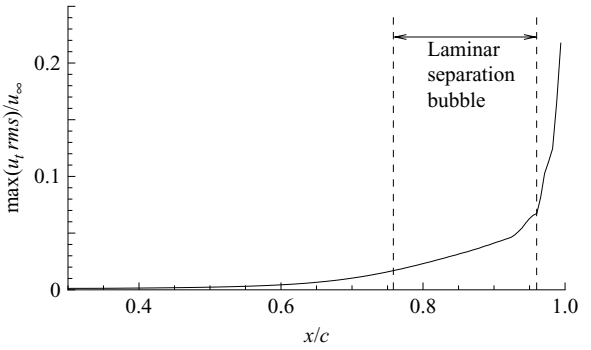

FIGURE 14. Case 1: evolution of the maximum of the *rms* of u_t in the boundary layer depending on the chordwise position on the pressure side.

For the calculations, some classical assumptions have been considered. First, the flow is assumed to be laminar and nearly parallel – in practice, this assumption is valid if the boundary-layer thickness increases slowly with respect to one instability wavelength. Secondly, the disturbances are assumed to remain small enough to be governed by the linear regime. The numerical method used to solve the iNS equations in a perturbation form is based on a Chebyshev collocation method (for more details see Schmid & Henningson 2001). The mean profiles were not modelled as in the previous studies, but simply interpolated from the DNS results on a one-dimensional grid deriving from the collocation point distribution.

5.1. *Pressure side*

Figure 14 displays the evolution of the maximum of the *rms* of u_t in the boundary layer along the pressure side. Before $x/c = 0.4$, the *rms* value remains very small. After the reattachment point, $x/c = 0.96$, a strong increase in the amplitude can be observed. This may be due to the interaction of the flows coming from the pressure and suction sides at the trailing edge. Therefore, the spatial analysis has been carried out for the mean profiles from $0.3\,x/c$ to $0.96\,x/c$.

On the pressure side, linear spatial stability analysis has been performed at more than 30 chordwise stations ranging from 30 % of the chord to the reattachment point. The results of selected (for the sake of clarity) profiles are shown in figure 15. Several remarks can be made about this figure: (i) curves are globally centred around the main tonal frequency of 830 Hz; (ii) the profiles corresponding to stations located inside the separation bubble (from 76 % to 96 % of the chord) present the largest spatial growth rate w_i; (iii) the curve at $x/c = 96$ % is significantly different from those in the separation bubble, indicating that there is a rapid change in the characteristics of the mean profile at the reattachment point. These results also make it possible to estimate the amplification ratio of the instability amplitude of a selected frequency between $x/c = 0.3$ and $x/c = 0.96$ as:

$$\frac{A(x)}{A(x_0)} = \exp\left(\int_{x_0}^{x} -\alpha_i(u)\,\mathrm{d}u\right), \tag{5.1}$$

where $\int_{x_0}^{x} -\alpha_i(u)\mathrm{d}u$ is usually referred to as the n-factor. The results of the calculations from $x_0/c = 0.3$ to $x/c = 0.96$ are shown on figure 16(a) for selected frequency modes between 400 and 1400 Hz with increments of 60 Hz. It can be seen that the most amplified frequency (845 Hz) is very close to the main tone noise frequency (830 Hz)

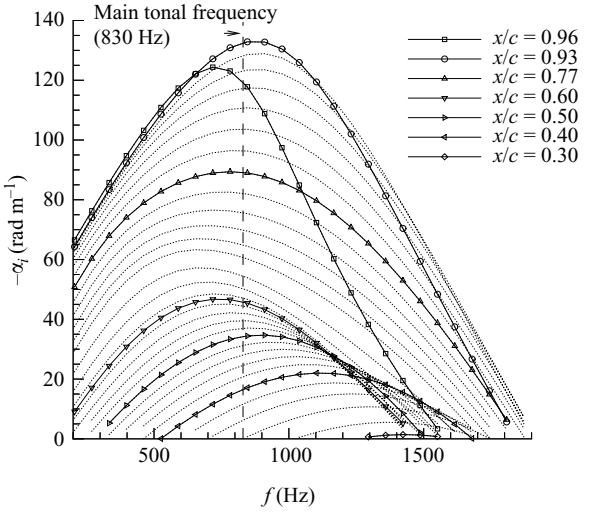

FIGURE 15. Spatial stability analysis results, spatial growth rates ($-\alpha_i$) depending on frequency (f) are displayed for several chordwise stations for Case 1 pressure side.

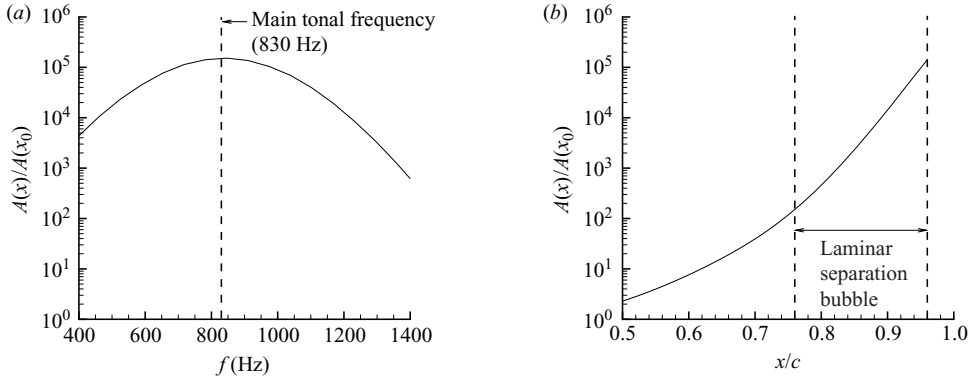

FIGURE 16. (*a*) Amplification of selected frequency modes from $x/c = 0.3$ to $x/c = 0.96$ in log scale, frequency increment: 60 Hz. (*b*) Amplification ratio depending on x for the most amplified frequency (845 Hz) in log scale.

considering the frequency resolution uncertainty (± 30 Hz). The calculations of Nash *et al.* (1999) led to similar results. It can therefore be concluded that the main tone noise frequency f_s is linked to the most amplified instability wave along the pressure side's boundary layer. The computation of the amplification ratio for different chordwise stations and the same x_0 shows that the most amplified frequency is constant and equal to 845 Hz from $x/c = 0.7$ to $x/c = 0.96$. The tone noise frequency is therefore selected before the boundary-layer separation. The mean flow for those chordwise stations is characterized by an inflection point. This indicates that the most amplified frequency is linked to an inviscid instability. McAlpine *et al.* (1999) made the same observations for the pressure side profiles that they analysed. In figure 16(*b*), the amplification ratio $A(x)/A(x_0)$ is displayed as a function of x for the most amplified frequency. As seen by Nash *et al.* (1999), the largest amplification occurs in the separation bubble.

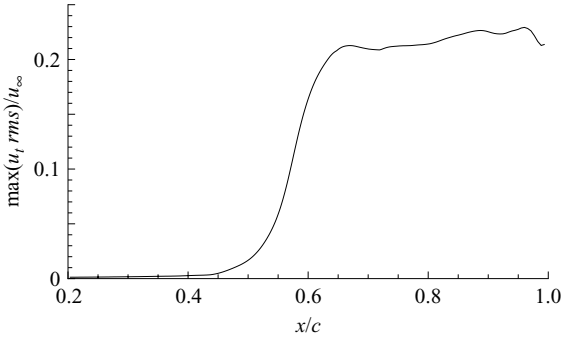

FIGURE 17. Case 1: evolution of the maximum of the *rms* of u_t in the boundary layer depending on the chordwise position on the suction side.

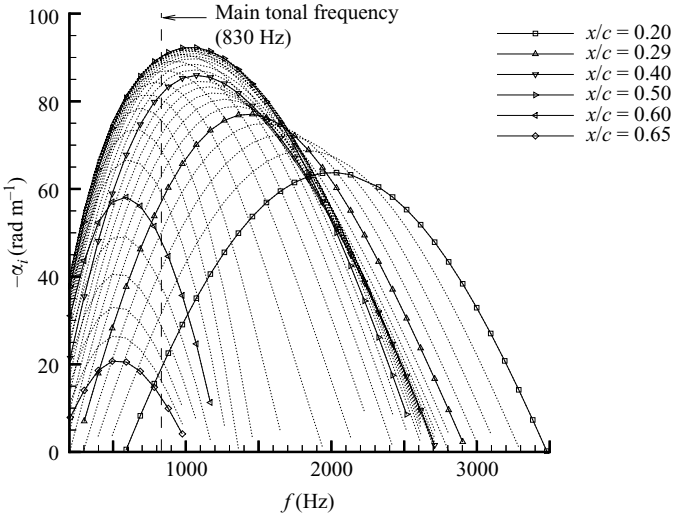

FIGURE 18. Spatial stability analysis results, spatial growth rates ($-\alpha_i$) depending on frequency (f) are displayed for several chordwise stations for Case 1 suction side.

5.2. *Suction side*

Figure 17 shows the maximum of the *rms* of u_t in the boundary layer depending on the chordwise position for the suction side. It can be seen that this quantity increases strongly between $x/c = 0.4$ and $x/c = 0.6$, whereas saturated levels are observed from $x/c = 0.65$. Therefore, the spatial analysis has been performed from $x/c = 0.2$ to $x/c = 0.65$.

The results of the spatial linear stability analysis for some mean profiles from 20 % and 65 % of the chord on the suction side for Case 1 are shown in figure 18. It can be seen that the maxima of the spatial growth rate are not centred around the main tonal frequency as was observed at the pressure side.

Figure 19(a) shows the result of the calculations of the amplification ratio $A(x)/A(x_0)$ computed from $x_0/c = 0.2$ to $x/c = 0.65$ for selected frequency modes between 200 and 3400 Hz, with increments of 95 Hz. It can be seen that the most amplified frequency, 975 ± 47.5 Hz, differs from the main tonal one, 830 Hz, with a relative error of about 15%. Considering the level of approximations done using linear instability analysis, such an error is usually acceptable for the prediction of

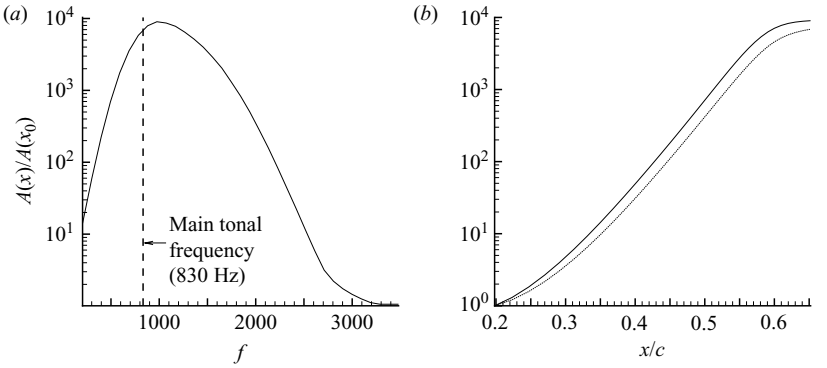

FIGURE 19. (*a*) Amplification of selected frequency modes from $x/c = 0.2$ to $x/c = 0.65$ in log scale for the suction side, frequency increment: 95 Hz. (*b*) Amplification ratio depending on x in log scale: ——, most amplified frequency (975 Hz); $\cdots$, tone noise frequency (830 Hz).

the most amplified frequency. For instance, McAlpine *et al.* (1999) considered that the tone frequency was the most amplified frequency of the pressure side in a case where the error was 23%. However, in our case, the mean flow did not require any modelling and is given directly by the numerical simulation. Moreover, the tone noise frequency and the most amplified frequency of the pressure side are in very good agreement. Therefore, it can be thought that the tone noise frequency is not the most amplified frequency at the suction side.

Figure 19*b* displays the amplification ratio $A(x)/A(x_0)$ as a function of x for the most amplified frequency (975 Hz) and for the tone noise one. It can be seen that the tone noise frequency is still strongly amplified throughout the boundary layer, even if it is not the most amplified one. This indicates that the boundary layer is highly receptive to external disturbances – such as acoustic waves – at this specific frequency, and explains why some instabilities at the same frequency are observed on the suction side (see figure 13*b*). This receptivity mechanism is a complex phenomenon whose study is beyond the scope of the present study.

5.3. *Conclusion*

The linear stability analysis of the mean flow on the pressure side has shown that the main tone noise frequency f_s is similar to the frequency of the most amplified perturbation from $x/c = 0.7$ to $x/c = 0.96$. It has also been pointed out that these perturbations are mainly amplified in the separation bubble. These results are similar to experimental measurements. The stability analysis reveals that the main tone noise frequency is not the most amplified one on the suction side. However, it is shown that the boundary layer of this side is highly receptive to the tone frequency. The mechanism for the main tone noise frequency, f_s, generation proposed by Nash *et al.* (1999) and McAlpine *et al.* (1999) is therefore assessed by the present direct numerical simulation results. The main tone frequency f_s is close to the most amplified one in the boundary layer of the pressure side, and is selected before the separation bubble where it is then strongly amplified. The interaction between the hydrodynamic fluctuations and the trailing edge acts as an acoustic source close to the trailing edge. The generated acoustic waves then excite instabilities on the pressure side, yielding a feedback-loop mechanism. A similar process might be *a priori* expected at the suction side. The main reason why the most amplified frequency at the suction side does not govern the main tone frequency is that the amplification ratio at the suction side is by

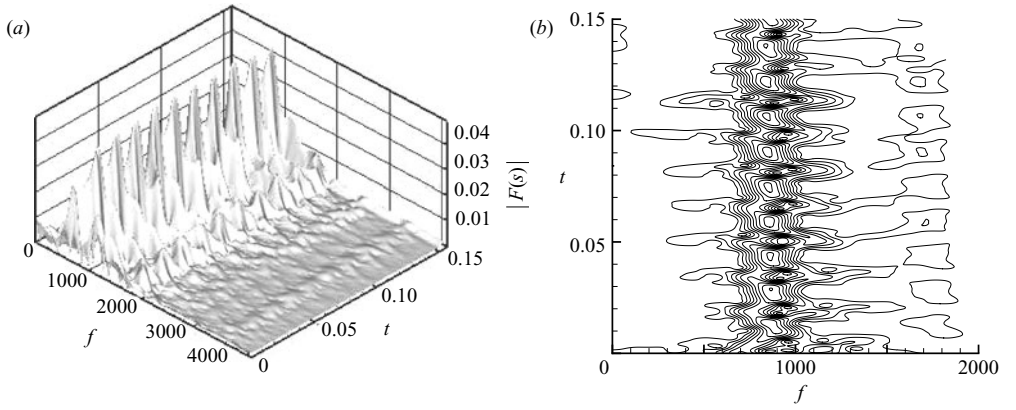

FIGURE 20. Windowed Fourier transform of the acoustic signal in point 1: (*a*) three-dimensional view; (*b*) two-dimensional view.

two orders of magnitude lower than the one at the pressure side. The receptivity of the boundary layer on the suction side explains the presence of disturbances having the tone noise frequency on this side. The interaction with pressure side perturbations remains to be investigated.

6. Discrete frequencies (f_n) generation

As shown by Arbey & Bataille (1983), two different contributions can be distinguished in the acoustic spectrum of the tone noise phenomenon: a broadband contribution centred on a main tone frequency f_s and several secondary discrete components f_n. The mechanism of f_s generation proposed by Nash *et al.* (1999) has been validated in the previous section. Arbey & Bataille (1983) are the only authors who proposed an explanation for the presence of the secondary discrete frequencies f_n, which has not been assessed using experimental data. Therefore, the present section is devoted to analysis of the generation of the discrete components f_n.

6.1. *Windowed Fourier transform*

Since the frequency resolution of the signal is high, the windowed Fourier transform tool (Gabor 1946) has been used to analyse the acoustic signal of Case 1 in more detail. This transform consists in analysing the frequency content of a signal around a time value t_0. To do so, the signal is multiplied by a symmetrical function with a compact support $b(t - t0)$, centred on t_0. The window function retained here is based on Hanning's function $h(t) = \cos^2(\pi t)$. It has been dilated such that its support is equal to 8 periods of the main tonal frequency of the spectrum. Figure 20 displays the result of the windowed Fourier transform computation over 33 periods of the main tonal frequency. An amplitude modulation of the main peak frequency around 850 Hz can be seen. The amplitude modulation is periodic and its associated frequency is estimated as 63.5 Hz, which is similar to the frequency spacing of the discrete peaks of the acoustic spectrum. The windowed Fourier transform therefore provides a new point of view for interpreting the discrete frequencies of the spectrum. It appears that there is only one emerging frequency, whose amplitude changes periodically. The fact that the measured modulated frequency, 850 Hz, is not exactly equal to the main tonal frequency, 830 Hz is only due to the limitation in the frequency resolution of the windowed Fourier transform approach, and it is therefore considered that

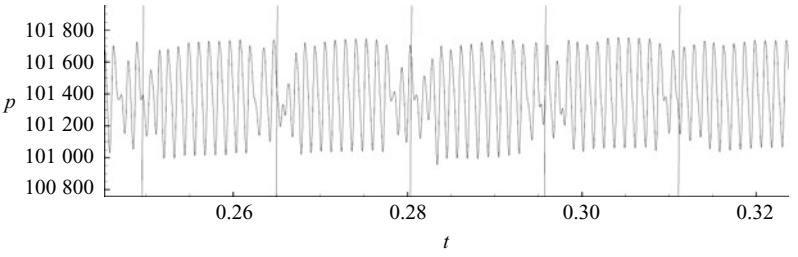

FIGURE 21. Part of the pressure signal at point 1, the regular distance between vertical lines is associated to a 64 Hz frequency.

the observed modulated frequency is the main tonal frequency. Figure 21 shows a part of the pressure signal on which the windowed Fourier transform was applied. The periodic variation of the signal amplitude can also be observed directly on this signal, with the same frequency as that predicted by the windowed Fourier transform analysis.

6.2. *Flow visualization*

In order to understand the origin of this phenomenon, the flow at the trailing edge has been visualized using two-dimensional field sampling. Snapshots are stored every 176 time steps during the Case 1 simulation. Therefore, 8 samples correspond to the period of the main discrete frequency. Some movies have been made, which make it possible to observe the noise-generation process. It is found that the high noise level radiation case and the low level one are characterized by two typical flow configurations in the trailing-edge region which can be observed in figures 22 and 23.

Each of these figures displays a two-dimensional view of the flow and two graphs. Figures 22(*b*) and 23(*b*) show the pressure levels in grey scale around the trailing edge and iso-values of vorticity in black line. The vorticity peaks are located on pressure minima. The extremities of the vertical line in the wake (dashed line) indicate the location of the two acoustic sources that are observed. The largest values of the *rms* pressure occur in these regions. The second vertical line indicates the trailing edge. The distance between the trailing edge and the source area is about one spatial wavelength of the vortex shedding pattern. This is in agreement with the observations of trailing-edge noise by Arbey (1981) and Gaudriot *et al.* (1982). Two horizontal dashed lines are also displayed. They are localized at 0.015 chord from the profile and from the symmetry axis of the airfoil. The pressure level on these lines can be observed figures 22(*a*) and 23(*a*): dashed lines and solid lines are related to the pressure side and the suction side, respectively. In figures 22(*c*) and 23(*c*), the instantaneous fluctuating pressure profile along the normal direction is displayed from the location of the two acoustic sources, showing the generated acoustic waves. Figure 22(*c*) shows the flow in a configuration of high noise level radiation. On the other hand, figure 23(*c*) shows only weak acoustic waves. The dipolar nature of the acoustic sources can be clearly seen: in both figures, regular pressure fluctuations are observed on the pressure side (from 90 % of the chord) and the suction side (from 50 % of the chord). This is consistent with the previous analyses of the mean and *rms* velocity profiles. The main difference between the two snapshots is the phase of the vortices at the trailing edge. A phase opposition occurs for the high noise configuration, whereas the pressure fluctuations exhibit phase-locking in the low noise configuration. This shows the significant role of the boundary-layer instabilities at the suction side in the tone noise phenomenon, whereas they have been neglected

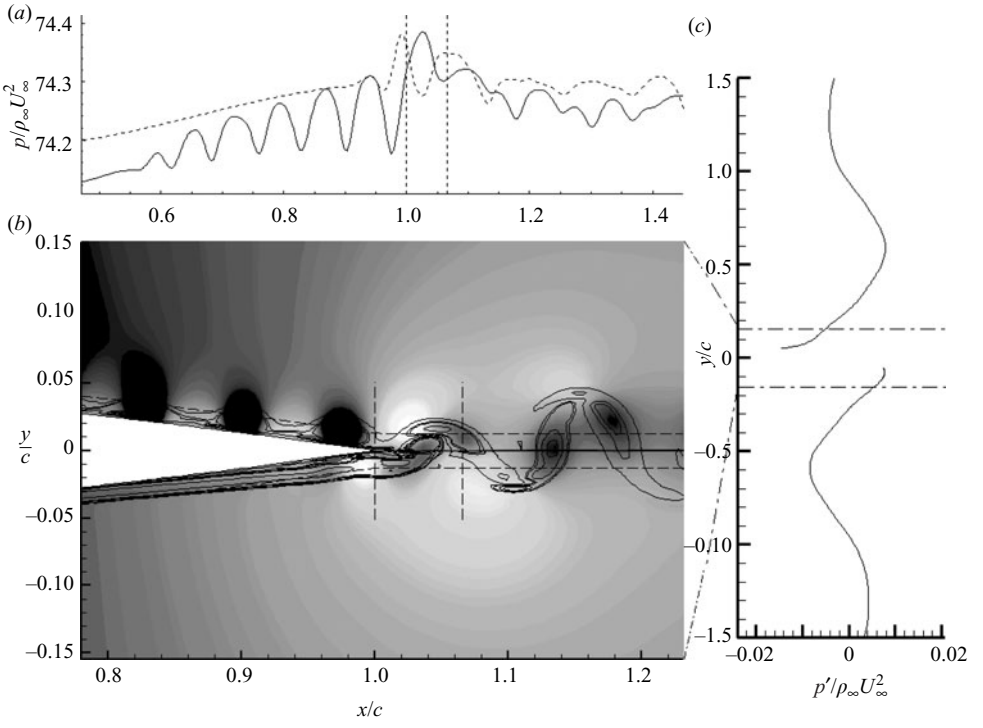

FIGURE 22. Flow configuration near the trailing edge for high noise level radiation case. (*b*) Pressure field in grey scale and iso-value of vorticity in black line. (*a*, *c*) One-dimensional extraction of the pressure field.

in the previous studies. The acoustic pressure amplitude is observed to depend on the instability phases at the trailing edge. In order to understand why the acoustic sound levels of the two configurations are so different, an analysis based on Lighthill's theory (1952) has been carried out, in order to compare the intensities of the Lighthill source terms in each case (not shown here). This study has, however, not allowed us to find the fundamental explanation of such a difference. Cabana, Fortune & Jordan (2006) studied a decomposition of the Lighthill source term in ten subterms. They observed with a direct numerical simulation of a two-dimensional temporal mixing layer that the essence of sound production relies on a subtle difference between the different subterms. Therefore, the study of the mechanism of sound generation of the two exhibited configurations requires an extensive study, which is beyond the scope of the present work. The transition of the flow from one configuration to the other has also been observed. Figure 21 shows that this transition corresponds to a fast bifurcation. On the top left-hand side of figure 24, the pressure field on the pressure side is displayed at several times just before the decrease of the acoustic wave amplitude. The distance between two vortices is regular except between two of them (marked with white lines). When arriving at the trailing edge, the distance between these two 'specific' vortices decreases. As a first consequence, the distance between the vortices becomes uniform, and as a second one, the vortex at the suction side becomes in phase with the one from the pressure side at the end of the sequence.

The three snapshots in figure 25 show the transition from a low noise level configuration toward a high noise level one. They have been sampled at every period

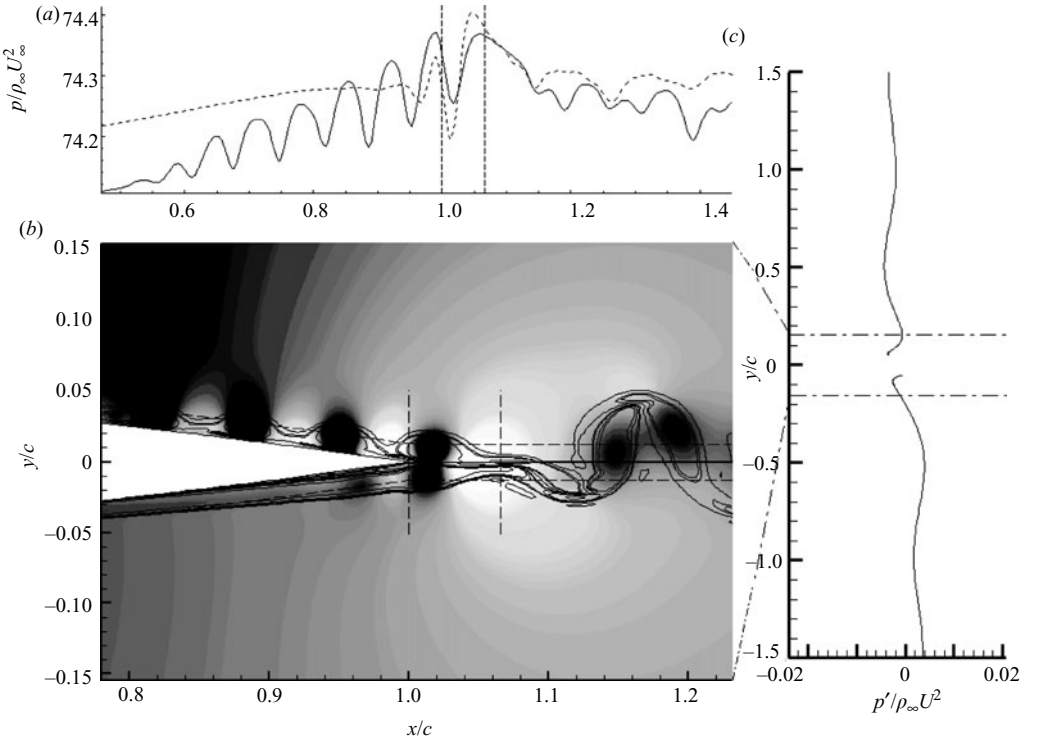

FIGURE 23. As for figure 22, but for low noise level radiation case.

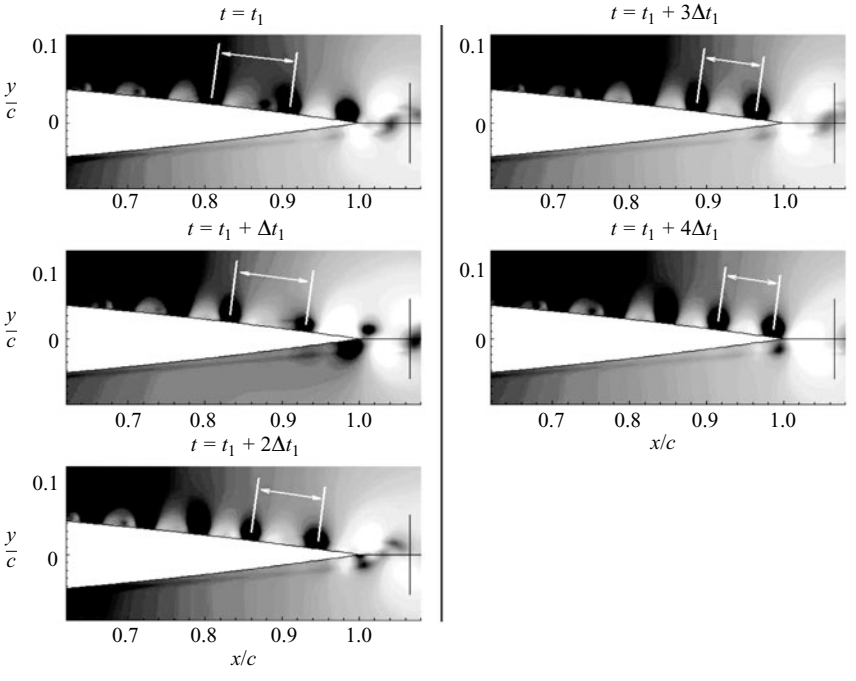

FIGURE 24. High noise level configuration to low one transition process. Pressure level in grey scale. Noise sources at the extremities of the vertical segment. $\Delta t_1 = 0.516\ c/a_0$.

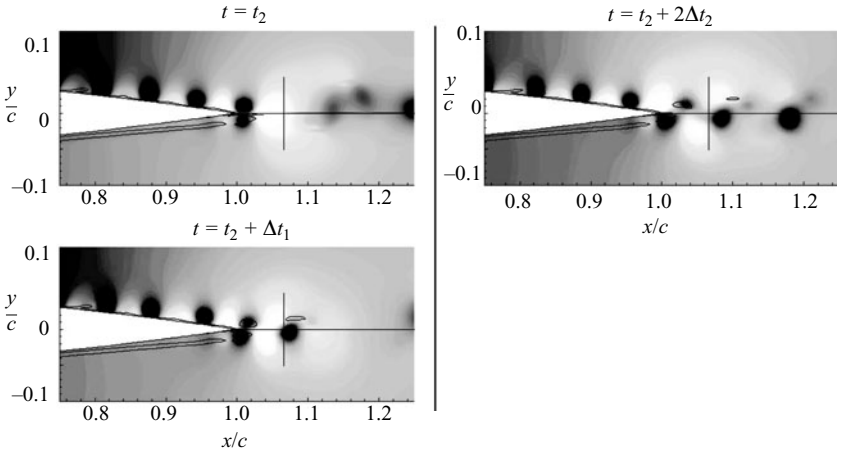

FIGURE 25. Low noise configuration to high noise configuration transition process. Pressure level in grey scale and iso value of vorticity in black line. $\Delta t_2 = 1.4\,c/a_0$, Δt_2 is the vortex shedding period at the pressure side.

of the vortex shedding at the pressure side, Δt_2. It is observed that the transition from low noise to high noise configuration requires only two periods to occur. This transition appears to be natural, and driven by the unstable equilibrium between two counter-rotating phase-locked vortices.

6.3. *Conclusion*

In this section, the origin of the secondary discrete frequencies f_n observed in the acoustic spectrum has been identified. They have been shown to be a consequence of a periodic modulation of the amplitude of the main tonal frequency, f_s. The period of this modulation is strictly equal to the regular spacing Δ_f between the secondary frequencies. Visualizations of the flow at the trailing edge reveal, respectively, that the amplitude of the acoustic signal is due to the phase difference of the vortices shed from the suction and pressure sides. The transition from a high acoustic radiation level to a low one is observed to be due to an irregular vortex shedding at the suction side, whereas the transition from the low to the high radiation configuration appears to be natural. This is consistent with the observation that periods with low-amplitude radiated acoustic waves appear suddenly and briefly in the acoustic pressure signal. The high noise level radiation state therefore seems to be the stable one, while the other appears to be a perturbation. This perturbation occurs with a period equal to the period of the amplitude modulation of the tone frequency. The reason for this regularity remains to be explained. Further investigations are necessary to clarify that point.

7. Discussion and concluding remarks

A study of the tonal noise phenomenon has been carried out via direct numerical simulation of the flow around a NACA0012 airfoil. For Case 1, it is shown that the acoustic spectrum of the noise generated by the flow exhibits the characteristics of the tone noise phenomenon: a main discrete frequency $f_s = 830\,\text{Hz}$ dominates the spectrum with secondary peaks with a uniform spacing of 64 Hz. For Case 2, the acoustic spectrum exhibits a broadband contribution centred around 260 Hz with

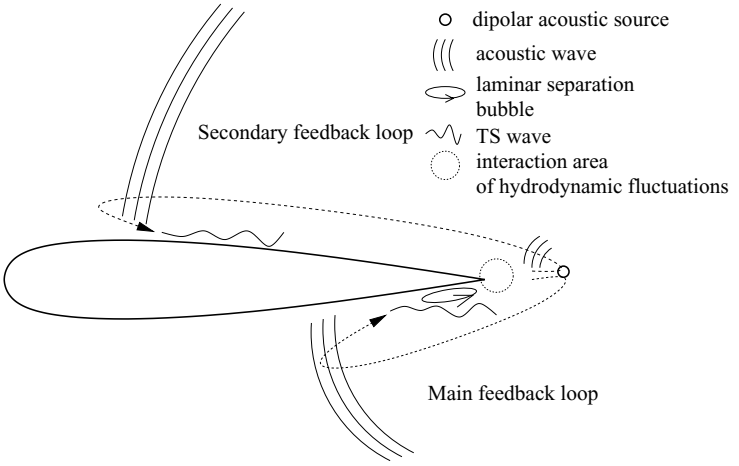

FIGURE 26. Scheme of the tonal noise mechanism.

a harmonic at 520 Hz, but no discrete frequencies are observed. So, as in several experimental studies referred to, it is observed that the noise generated by the flow around an airfoil can exhibit very different features depending on the parameters of the configuration. In both cases, the acoustic source is of a dipolar nature and located in the wake, close to the trailing edge, which is a typical feature of trailing-edge noise (Arbey 1981; Gaudriot *et al.* 1982). It is observed that the main difference in the mean flow between the two configurations is the presence of a separation bubble for Case 1 on the pressure side near the trailing edge (between $x/c = 0.76$ and $x/c = 96$). The existence of this recirculation bubble had already been identified as a necessary condition for the tone noise phenomenon to occur (Lowson *et al.* 1994). The computed *rms* velocity profiles at this location present the same features as the experimental ones (Nash *et al.* 1999). A space/time Fourier transform of the wall pressure fluctuations on the pressure side near the trailing edge reveals the existence of two types of fluctuation: hydrodynamic and acoustic. The spectra of both fluctuation types exhibit the tone noise peak. A linear spatial instability analysis has shown that the most amplified TS waves on the pressure side, from $x/c = 20\,\%$ to $x/c = 96\,\%$, were centred on the main tone noise frequency, $f_s = 830$ Hz. The computed spatial amplification ratio shows that the main tone noise frequency is close to the most amplified frequency along the pressure side. In particular, it was shown that the tone frequency is selected by the boundary layer before the separation bubble, which then acts as an amplifier. Therefore, the mechanism proposed by Nash *et al.* (1999) for the generation of the main tone frequency f_s has been assessed by the present numerical results. This mechanism is based on a feedback loop between the boundary layer on the pressure side and the acoustic source, owing to the interaction of the TS waves with the trailing edge (see figure 26: main feedback loop). However, this feedback mechanism cannot explain the existence of the regularly spaced discrete frequencies, f_n, around the main tone one f_s. A time/frequency Fourier analysis of the acoustic signal has shown that they originate from a periodic amplitude modulation of f_s, with a period equal to the frequency step between each f_n. The visualization of the flow at the trailing edge allowed us to observe this phenomenon. More precisely, it is noted here that the phase difference between the hydrodynamic fluctuations on the pressure and suction sides has a significant impact on the amplitude of the generated acoustic waves. A 180° phase shift induces a high-amplitude radiated acoustic wave

while phase-locking results in a weak acoustic radiation. The fundamental reason for the sound intensity difference between the two configurations remains unclear, and is beyond the scope of this paper. An interaction between the most amplified frequencies at the pressure side and at the suction side might be a possible explanation for the periodic bifurcation from one configuration to the other one – the difference between these two frequencies is of the order of $2\Delta_f$ – but this point remains to be investigated. So, it is shown in this paper that the instabilities from the suction side also play a role in the tone noise generation, although they have been neglected since the experimental work of Arbey & Bataille (1983). They belong to a second feedback loop that modulates the amplitude of the main one. The mechanisms for tone noise generation are schematized in figure 26.

The authors would like to thank G. Casalis for interesting and useful discussions on boundary-layer instabilities. L. Lesshafft and F. Richez are also acknowledged for their help in the development of the linear instability analysis code.

REFERENCES

Alam, M. & Sandham, N. D. 2000 Direct numerical simulation of 'short' laminar separation bubbles with turbulent reattachment. *J. Fluid Mech.* **403**, 233–250.

Arbey, H. 1981 Contribution à l'étude des mécanismes de l'émission sonore de profils aérodynamiques placés dans des écoulements sains ou perturbés. PhD thesis, Université Claude Bernard Lyon I.

Arbey, H. & Bataille, J. 1983 Noise generated by airfoil profiles placed in a uniform laminar flow. *J. Fluid Mech.* **134**, 33–47.

Archibald, F. S. 1975 The laminar boundary layer instability excitation of an acoustic resonance. *J. Sound Vib.* **38**, 387–402.

Brooks, T. F., Pope, D. S. & Marcolini, M. A. 1989 Airfoil self noise and prediction. *NASA Ref. Pub.* 1218.

Cabana, M., Fortune, V. & Jordan, P. 2006 A look inside the Lighthill source term. In *12th AIAA/CEAS Aeroacoustics Conference. AIAA Paper* 2006-248.

Clark, L. T. 1971 The radiation of sound from an airfoil immersed in a laminar flow. *Trans. ASME J. Engng Power* **93**, 366–376.

Desquesnes, G., Terracol, M., Manoha, E. & Sagaut, P. 2006 On the use of a high order overlapping grid method for coupling in CFD/CAA. *J. Comput. Phys.* **220**, 355–382.

Fink, M. R. 1975 Prediction of airfoil tone frequencies. *J. Aircraft* **12**, 118–120.

Fink, M. R. 1978 Fine structure of airfoil tone frequency. *95th Meeting Acoust. Soc. Am.* Paper H3.

Gabor, D. 1946 Theory of communication. *J. IEEE* **93**, 429–457.

Gaudriot, L., Hellion, A., Bequet, B. & Arbey, H. 1982 Analyse du bruit de profil par réseaux de capteurs proches ou lointains. *Rev. d'Acoust.* **63**, 208–210.

Goldstein, M. E., Leib, S. J. & Cowley, S. J. 1987 Generation of Tollmien–Schlichting waves on interactive marginally separated flows. *J. Fluid Mech.* **181**, 485–517.

Henry, C. 1975 Solution numérique par une méthode de singularités du problème de l'écoulement compressible sur des surfaces de courant axi-symetriques. PhD thesis, Université Claude Bernard Lyon I.

Hersh, A. S. & Hayden, R. E. 1971 Aerodynamic sound radiation from lifting surfaces with and without leading edge serrations. *NASA Contractor Rep.* CR-114370.

Koch, W. 1985 Local instability characteristics and frequency determination of self-excited wake flows. *J. Sound Vib.* **99**, 53–83.

Lighthill, M. J. 1952 On sound generated aerodynamically. I. General theory. *Proc. R. Soc. Lond.* A **211**, 564–587.

Longhouse, R. E. 1977 Vortex shedding of low tip speed axial flow fans. *J. Sound Vib.* **53**, 25–46.

Lowson, M. V., Fiddes, S. P. & Nash, E. C. 1994 Laminar boundary layer aeroacoustic instabilities. *AIAA Paper* 94-0358.

Lowson, M. V., McAlpine, A. & Nash, E. C. 1998 The generation of boundary layer instability noise on aerofoils. *AIAA Paper* 98-0626.

McAlpine, A., Nash, E. C. & Lowson, M. V. 1999 On the generation of discrete frequency tones by the flow around an aerofoil. *J. Sound Vib.* **222**, 753–779.

Mari, C., Jeandel, D. & Mathieu, J. 1976 Méthode de calcul de couche limite turbulente compressible par transfert de chaleur. *Intl J. Heat Mass Transfer* **19**, 893–899.

Na, Y. & Moin, P. 1998 Direct numerical simulation of a separated turbulent boundary layer. *J. Fluid Mech.* **374**, 379–405.

Nash, E. C. & Lowson, M. V. 1995 Noise due to boundary layer instabilities. CEAS/AIAA Aeroacoustics Conference, Munich, Paper 95–124.

Nash, E. C., Lowson, M. V. & McAlpine, A. 1999 Boundary-layer instability noise on aerofoils. *J. Fluid Mech.* **382**, 27–61.

Obremski, H. J., Morkovin, M. V., Landahl, M., Wazzan, A. R., Okamura, T. T. & Smith, A. M. O. 1969 A portfolio of stability characteristics of incompresible boundary layers. *AGARDograph* 134.

Paterson, R. W., Vogt, P. G. & Fink, M. R. 1972 Vortex noise of isolated airfoils. *AIAA Paper* 72-656.

Schmid, P. J. & Henningson, D. S. 2001 *Stability and Transition in Shear Flows*. Springer.

Sharland, I. J. 1964 Sources of noise in axial flow fans. *J. Sound Vib.* **1**, 302–322.

Shen, S. F. 1954 Calculated amplified oscillations in the plane Poisseuille and Blasius flows. *J. Aeronaut. Sci.* **21**, 62–64.

Smith, D. L., Paxson, R. P., Talmadge, R. D. & Hotzo, E. R. 1970 Measurements of the radiated noise from sailplanes. *Rep.* TM-70-3-FDAA, US Air Force Flight Dynamics Laboratory.

Stewartson, K., Smith, F. T. & Kaups, K. 1982 Marginal separation. *Stud. Appl. Maths* **67**, 45–61.

Sunyach, M., Arbey, H., Robert, D., Bataille, J. & Comte-Bellot, G. 1973 Correlations between far-field acoustic pressure and flow characteristics for a single airfoil. *AGARD Conf. 131 Noise Mechanisms*, paper 5.

Tam, C. K. W. 1974 Discrete tones of isolated airfoils. *J. Acoust. Soc. Am.* **55** (6), 1173–1177.

Thompson, K. W. 1987 Time dependant boundary conditions for hyperbolic systems. *J. Comput. Phys.* **68**, 1–24.

Visbal, M. R. & Gaitonde, D. V. 2002 On the use of higher-order finite-difference schemes on curvilinear and deforming meshes. *J. Comput. Phys.* **181**, 155–185.